RESEARCH PAPER

CrossMark

Application of different simulation approaches to numerically optimize high-frequency mechanical impact (HFMI) post-treatment process

Clément Ernould[1] · Jan Schubnell[1] · Majid Farajian[1] · Andreas Maciolek[1] · David Simunek[2] · Martin Leitner[2] · Michael Stoschka[2]

Abstract

The weld seam is generally the weak point of welded mechanical parts subject to fatigue loading. For this issue, a post-weld mechanical surface process called high-frequency mechanical impact (HFMI) was developed. This process combines both mechanical effects and a weld geometry improvement by generating compressive residual stresses and making a smoother transition between the base plate and the weld. Benefits of the process are statistically proven by numerous fatigue test results. Finite-element method (FEM) based numerical simulations of the process have been developed to estimate the material state after treatment. Good agreements with experimental results were obtained. Until present, rebounds of the pin between each primary impact have not been overlooked by such simulations. To discuss their eventual effects, signal of strain gauges glued on the pin was processed. A typical impact pattern of the pin kinetic during HFMI treatment could be identified and then implemented in a pre-existing FEM model. Numerical simulations were conducted using recently developed non-linear combined isotropic-kinematic hardening law with strain-rate dependency according to Chaboche und Ramaswamy–Stouffer models. These hardening laws were calibrated for S355 J2 mild steel. The simulation procedure was performed for flat specimen and representative butt weld joint.

Keywords Welding · Fatigue strength improvement · High-frequency mechanical impact (HFMI) treatment · Finite-element simulation

1 Introduction

The advantages of removing the potential threats of unwanted (tensile) residual stresses and exploiting the beneficial (compressive) residual stresses by mechanical treatments are already known in welding communities. The innovation of locally modifying the residual stress state in welded components by the use of an ultrasonic hammering technology is widely attributed to E. Statnikov [1]. Nowadays, there are different high-frequency mechanical impact (HFMI) tool

manufacturers and service providers, but the operating principle is always identical: an indenter is accelerated against a component's surface with high frequency (> 90 Hz), causing local plastic deformation and residual stresses.

In this context, HFMI as post-weld treatment is a statistically proven method to increase the fatigue life of welded joints [2–13]. During this process, a hardened cylindrical metal pin with a spherical tip impacts the weld toe surface with high frequency and induces local plastic deformation. The resulting surface compressive residual stresses, the reduced notch effect at the weld toe, and the local work hardening of the material are the main reasons for the increased fatigue strength [13, 14]. The interactions between these effects and their single influence to the fatigue strength improvement of HFMI-treated welded joints are still not completely understood.

1.1 Overview of numerical simulations from the literature

To estimate the increase of fatigue life by damage- and fracture mechanical local approaches, it is absolutely necessary

---

✉ Jan Schubnell
jan.schubnell@iwm.fraunhofer.de

[1] Fraunhofer Institute for Mechanics of Materials IWM, Freiburg, Germany

[2] Montanuniversität Leoben – Chair of Mechanical Engineering, Leoben, Austria

that the numerical calculations describe the induced residual stress field accurately. Numerical simulation of the HFMI-process has thus been recently investigated by [15–28]. [16–22] focused on the influence of the mesh size, choice of friction model, overlapping of tool indentations, and applicable boundary conditions on the numerical simulations.

Most of the numerical simulations are performed using the commercial software Abaqus© Explicit [16, 18–21, 24, 25, 27, 28], and they can be divided into two categories. Numerical simulations are either displacement-controlled simulations (DCS) [15–17, 19, 21, 22, 25] or force-controlled simulations (FCS) [16, 18, 20–22, 24, 27, 28]. For DCS, pin displacement is set so that the permanent indentation depth u is between 0.1 to 0.25 mm [15–17, 21]. For FCS, pin impact velocity varies from 1 [20] to 5 m/s [26, 28] but it is generally around 3 m/s [20–22, 24, 26, 27]. FEM model is mostly a three-dimensional half symmetric models, and the bottom of the treated specimen is clamped. A tangential friction coefficient between the pin and the specimen of 0.15 [15, 16, 21, 22, 25], 0.25 [20, 24, 29] or 0.5 [18, 26] is assumed. Pin is either modeled as a rigid [16, 19, 21, 22, 24, 25, 27–29] or a linear elastic [15, 17, 18, 21, 22, 26] body. A rigid pin reduces computational effort.

[24, 29] investigated the effects of the distance between indentations as well as the influence of the pin geometry and impact velocity on the residual stress field in a ultrasonic impact treatment (UIT)-treated 2024 aluminum alloy. They used a single-impact and a two-impact model [29] or simulated several parallel treatment lines [24]. Both highlighted that over a threshold distance, residual stress field generated by an impact is only slightly influenced by adjacent impacts. When distance is decreasing, maximum compressive residual stress increases and is located between impact locations. If this increase is however marginal at lowest distances, compressive residual stress field increases significantly [29]. For HFMI simulations, an overlapping between two consecutive impacts (feed rate) of 0.2 mm [16, 20–22, 27], 0.4 mm [16, 19–22, 24–26], or 0.8 mm [15] is

commonly used. According to [19], 0.4 mm shows the best compromise between calculation effort and achieved geometry for DCS. However, for FCS, a higher number of impacts are needed to reach similar values for u [21]. In all these studies, the pin has a tip radius R of 1.5 to 3 mm.

1.2 Influence of hardening law and strain-rate dependency

Effects of HFMI treatment are investigated on base material plates [15, 16, 19–21, 24, 25] or welded joints [15, 17–19, 26, 27]. S355 steel grade (or similar) has been investigated by [15–17, 19, 21, 22] assuming isotropic [15, 16, 19, 25], kinematic [17], or combined isotropic-kinematic [16, 19, 21, 22, 25] hardening law. Combined isotropic-kinematic hardening laws from [16, 21, 22, 25] are based on Chaboche [31] or Johnson–Cook [32] models.

Residual stress field strongly depends on the chosen hardening law [17, 21]. Residual stresses at the surface may significantly vary whether isotropic or kinematic is assumed [17]. Up to about 1.5-mm depth, isotropic hardening is dominant [21, 22] and a simple isotropic hardening gives qualitatively sufficient result up to 0.8-mm depth [25]. Kinematic hardening is however essential to take material softening during cyclic loading into account [19] as it is the case along the longitudinal direction of the groove achieved by HFMI treatment [21, 22]. For depth higher than 1.5 mm (low plastic strains), kinematic hardening has a higher influence [21, 22]. Higher accuracy, especially at larger depths [25], is thus obtained with combined isotropic-kinematic hardening law [21, 22, 25]. In the investigated case of flat S355 specimen, attempts to fit experimentally determined residual stress field with numerical simulation results led up to best agreements when using a combined isotropic-kinematic and strain-rate-dependent hardening law by DCS [21, 22].

Fig. 1 Original strain gage signal (black) and results after filtering (orange) and following amplification (red)
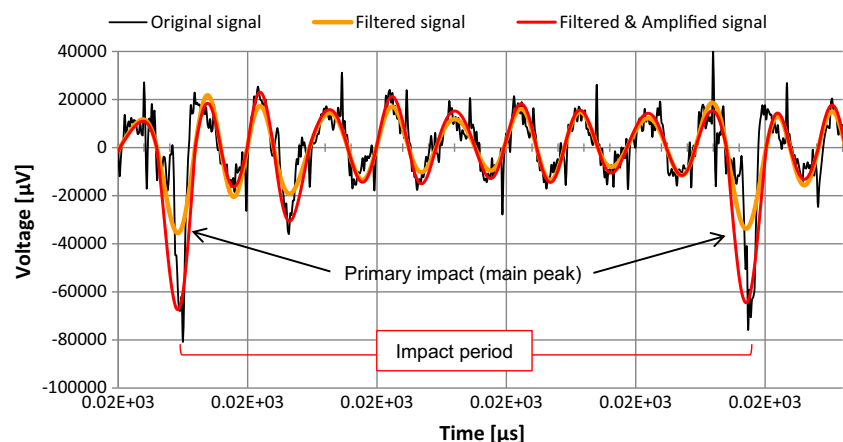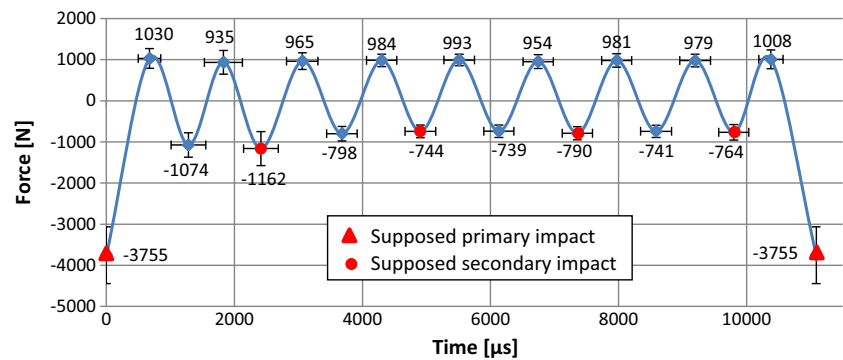
1.3 Manually versus automatically performed HFMI treatment

HFMI treatment can be performed either manually or using a robotic arm. However, robot assistance has not been investigated much yet. Yekta et al. [11] studied the influence of the UIT quality on fatigue by under, proper, and overtreating specimens in a manual or robotic way. A high degree of improvement was achieved in all cases, what shows that UIT is relatively robust for the investigated range of treatment conditions. Le Quilliec [23] highlighted that when using a robotic assistance, benefits of the HFMI treatment may strongly decrease if the pin incidence angle and impact location do not adapt to the local variation of the weld. Inappropriate contact is likely to generate folds if the weld toe itself is firstly impacted [23, 30]. Simunek et al. [19] performed HFMI treatment manually and using a clamped device. Scatter band of the maximum contact force between the pin and the specimen during impact was 50% narrower with the clamped tool.

Globally, higher repeatability and control of the process parameters are expected with robotically assisted HFMI treatment. A clamped tool would probably lead to higher and steadier transient forces. One of the most critical aspects would be on the capability of robots to take into account local variations of the weld toe geometry. If greater use of robots is practicable on production lines, HFMI treatment is mostly manually performed on large structures welded or repaired on-site like bridges, wind turbines, or ship and sometimes

underwater like pipelines and offshore platforms subject to severe stress corrosion-cracking conditions.

Prediction of the effects of the HFMI treatment for some given process conditions is central in the current research effort. In parallel, the stability of the treatment conditions, in particular during manual treatment, needs to be estimated. In this sense, this article presents a continuation of the work from [19, 21, 22] and introduces a method for a better description of the pin kinetic during HFMI treatment. Differences between a clamped or by operator handle tool are investigated. Results are implemented in Abaqus© Explicit in order to run and compare both displacement and FCS using the latest developed material hardening laws.

2 Comparison and analysis of strain gage measurements

2.1 Processing of strain gage signal

Strain gage measurements by Foehrenbach [21, 22] using a pneumatic PITec Weld Line 10 device with an operative pressure of 6 bar and a frequency of 90 Hz are processed by Ernould [33] by means of Fourier analysis. Sampling frequency f_s was 40 kHz. The analyses of these measurements are only performed for this specific pneumatically powered tool. It should be noticed that the results could significantly differ for other kinds of tools. A four-step processing of the average signal of

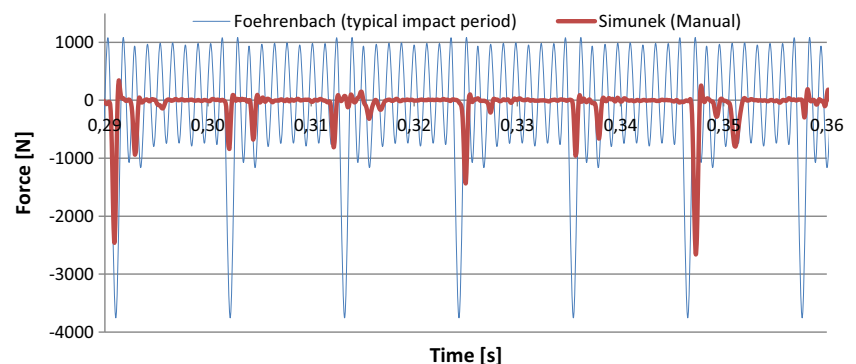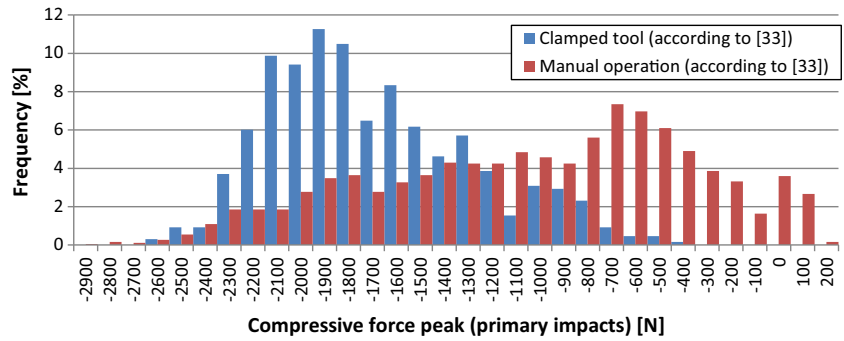Fig. 3 Strain gage measurements during manual HFMI treatment

Fig. 4 Distributions of compressive force peaks for manually and automatically performed HFMI treatment

the two strain gages is performed under MS Excel 2010 using VBA-macro programming. A typical impact period is shown in Fig. 1. Smoothing of the signal highlights both primary and secondary impacts and makes it easier to analyze thereafter.

For $k = 0, \ldots, N-1$

$$X_k = \sum_{n=0}^{N-1} x_n \cdot e^{-\frac{2\pi \cdot i}{N} k \cdot n} \tag{1}$$

$$x_n = \frac{1}{N} \sum_{k=0}^{N-1} X_k \cdot e^{\frac{2\pi \cdot i}{N} k \cdot n} \tag{2}$$

$$f_e = \frac{1}{N \cdot t_s} \tag{3}$$

$$f_k = k \cdot f_e \tag{4}$$

x_k	kth value of the temporal signal
X_k	kth value of the DFT
N	Number of samples
f_k	Frequency corresponding to the complex X_k
f_e	Frequency resolution
f_s	Sampling frequency
N	Number of samples
t_s	Sampling time

The discrete Fourier transform (DFT) (Eq. 1) is firstly computed according to the fast Fourier transform (FFT) algorithm proposed by Cooley and Tukey [32]. $N = 131{,}072$ samples are used so the frequency resolution is $f_e = 0.3$ Hz

(Eq. 3). As signal is real, its spectrum is symmetric about 20 kHz (half of the sampling frequency). Two frequencies stand out from the half-spectrum, 90.03 Hz and 816.36 Hz. In agreements with process parameters, the first one corresponds to primary impacts (highest peaks on Fig. 1). The second frequency is the mean frequency of the oscillations composing the filtered signal.

Spectrum is then filtered by setting $X_k = 0$ if $f_k > 1.2$ kHz (Eq. 4) or $|X_k| < 500{,}000$. The filtered signal (orange curve, Fig. 1) is the real part of the inverse DFT (Eq. 2) computed form the filtered spectrum according to the inverse FFT (IFFT) algorithm [32]. As filtering is responsible for signal attenuation, especially as far as primary impacts are concerned, the filtered signal is finally amplified (red curve, Fig. 1). An amplification factor is locally computed on each domain where the sign of the filtered signal remains unchanged.

2.2 Study of the process repeatability

As the strain gage signal seems to be quite periodic, the filtered and amplified signal is divided into impact periods. An impact period consists of a main peak and its following oscillations (Fig. 1). For each impact period, its duration and information relative to each peak (extremum, duration) are measured. A total number of 294 impact periods were analyzed for conducting a statistical analysis. It showed a high repeatability of the HFMI treatment as the different investigated values approximately follow a normal distribution

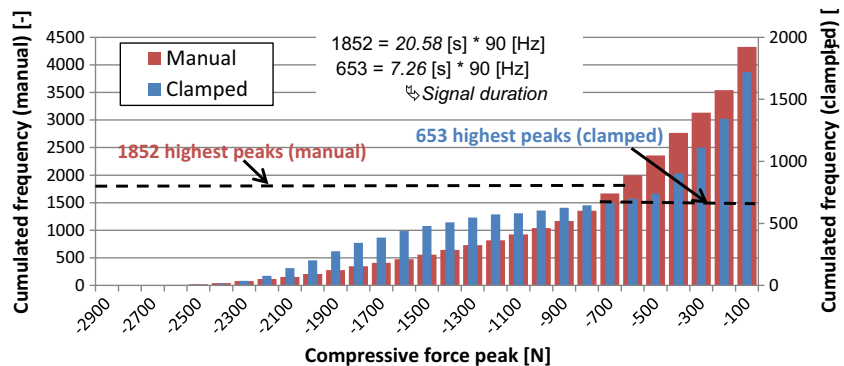**Fig. 5** Compressive force peaks distributions

Table 1 Maximum contact force during primary impacts determined using different approaches in terms of absolute values

	According to Ernould [33]				According to Simunek [19]			
	Max. (N)	Min. (N)	Mean (N)	St. dev. (%)	Max. (N)	Min. (N)	Mean (N)	St. dev. (%)
Manual	− 191	− 2915	− 1079	61	− 638	− 2915	− 1249	42
Clamped	+ 200	− 2678	− 1748	24	− 646	− 2678	− 1746	27

with a standard deviation about 20% for peaks extremum and 8% for peak duration. A typical impact period is thus identified (Fig. 2). Error bars correspond to the standard deviation, and voltage is converted into force.

This typical period is no more and no less than the mean periodic pattern composing the signal. It has a frequency of 90.18 Hz (± 0.5%), and it is composed of one main peak and eight secondary oscillations. The maximum of the main compressive force peaks amounts in terms of absolute value 3755 N (± 18%) which is consistent with the average maximum contact force of 3300 N determined by Foehrenbach [21, 22]. Difference is mainly caused by different strain gage calibration according to [33] which could lead to higher force values.

2.3 Influence of the tool fixation on impact forces

Strain gage measurements were carried out by Simunek et al. [19] on butt joints of S355 steel using the same device and process parameters as Foehrenbach [21, 22]. They performed the treatment manually and by clamping the HFMI device between two jaws. Qualitatively, the strain gage signal (Fig. 3) does not present as much oscillations as the one from [21, 22, 33] (Fig. 1). which might be due to the lower sampling frequency of 9600 Hz.

They showed that the scatter band of the compressive force peaks is 50% narrower when the device is clamped (1.5 to 2.25 kN) (Fig. 4). The mean value of those peaks was nearly the same in both cases. In the continuation of their work, main compressive force peaks are investigated again. Two approaches are used to identify primary impacts. The first one, according Simunek [19, 34], assumes that primary impacts correspond to the highest values of the compressive force peak distribution (Fig. 5). The second one according to Ernould [33] enforces a condition on the time interval between two consecutive main peaks. Their frequency of occurrence has to be 90 ± 10 Hz.

Results are summarized in Table 1. Both methods give similar results. Smaller and even positive extremum values are obtained with the second method as no significant compressive peak may be present in the restricted temporal range (neighborhood 0.36 s on Fig. 3 for instance). As expected, a clamped tool leads to about 40–60% higher compressive force peaks. This difference is clearly illustrated on Figs. 4 and 5. In agreements with the observation from [19], scatter band is significantly wider during manual treatment. According to the second method, the frequency of primary impacts amounts 89.6 Hz (± 6%) during manual treatment and 89.4 Hz (± 3%) with a clamped tool. Such results confirm the high reliability of the HFMI device highlighted in [33] as well as the higher repeatability of the process thanks to clamping.

Fig. 6 3D scan of the groove (**a**). Height with respect to the lowest measured value (**b**). Height profile along the broken line (**c**)
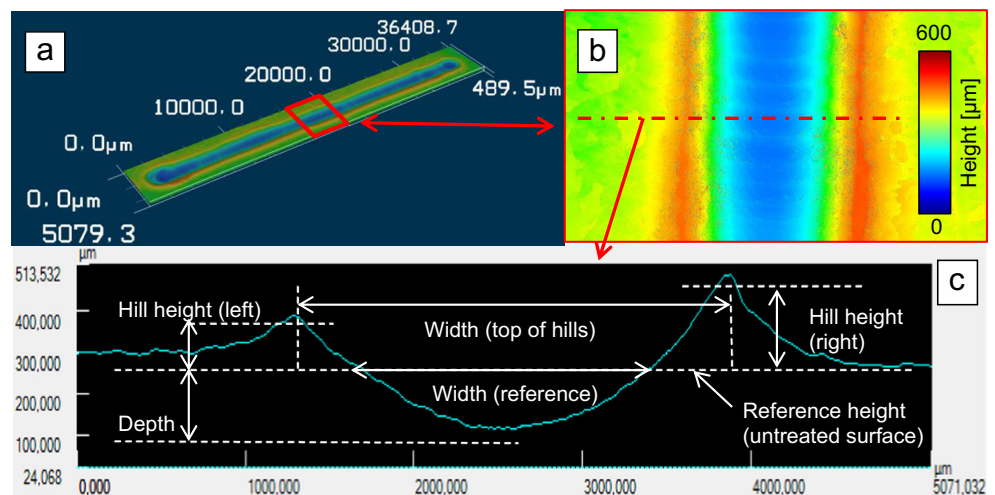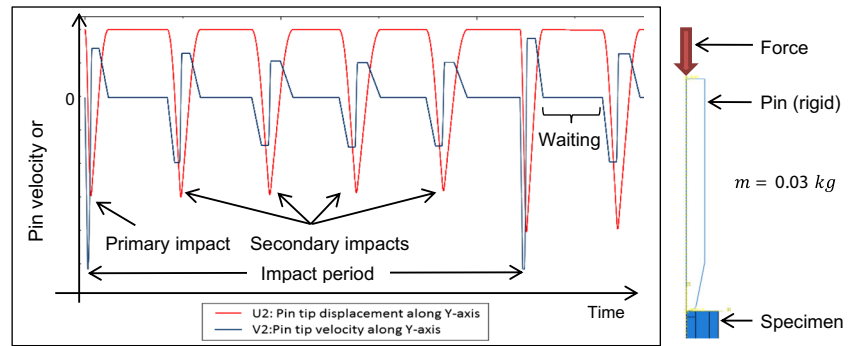
3 Simulation of the HFMI process on S355 steel sheets

Finite element method (FEM) model developed by Foehrenbach [21, 22] is reused to conduct FCS of the HFMI process. The latest developed and calibrated material models as well as secondary impacts are implemented by means of Abaqus© user subroutines. Influence of the pin kinetic and the material model calibration are investigated.

3.1 Experimental characterization of the specimens

In order to get validation values, a HFMI-treated sheet of S355 J2 (10-mm thickness) is experimentally characterized. The specimen was manually treated along a path of 30 mm using the same treatment conditions as for strain gage measurements. A pin with a tip radius of 2 mm and a travel speed of 12 cm/min (recommended by the constructer) were used. The treatment was repeated once, twice, and thrice at different paths.

Residual stresses (Figs. 9 and 10) were determined at the groove center by means of X-ray and neutron diffraction up to a depth of 5 mm [21, 22]. Measuring volume for neutron diffraction was $0.5 \times 1 \times 1$ mm^3 for the transverse and normal directions and $1 \times 1 \times 1$ mm^3 in the longitudinal direction. Groove topography is studied by scanning the specimen with 3D laser microscope (Fig. 6a–b) using a resolution of 1 μm. Groove dimensions are averaged by considering four height profiles (Fig. 6c). Finally, micro-hardness mapping in the cross section of the groove was realized.

Residual stresses at the surface were respectively − 200 and − 400 MPa along the transverse and longitudinal direction, and they turn into tensile at a depth of 2.6 and 3 mm. Maximum compressive residual stress of − 550 MPa is obtained at 0.8-mm depth in the transverse direction. The groove is about 0.16 mm deep and 2.2 mm wide (top of hills). The ratio between the two definitions of the groove width is around 1.4 what is consistent with the pin tip geometry [33]. Hills are 0.12 ± 0.02 mm high.

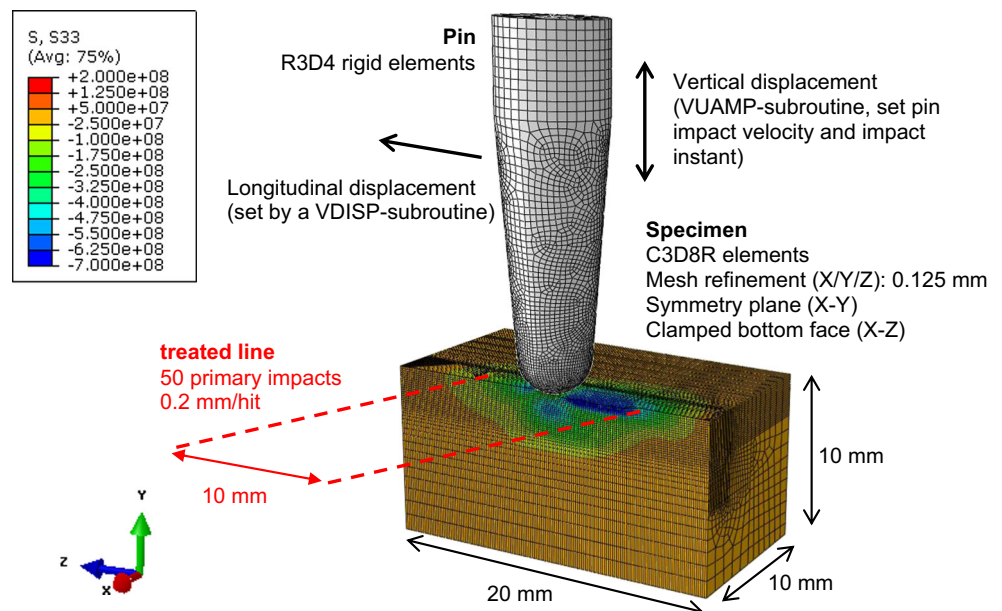**Fig. 8** 3D finite-element from [16, 22, 33] model for the numerical simulation of the HFMI process

Table 2 Simulated schemes for pin kinetic

Pin kinetic scheme		50SP	50HS V2475	50HS V3229
Impact velocity Vi (m/s)	Primary impact	2.745	2.745	3.229
	Secondary impact n°1	1.037	–	–
	Secondary impact n°2	0.762	–	–
	Secondary impact n°3	0.793	–	–
	Secondary impact n°4	0.776	–	–
Total kinetic energy (J)		0.156	0.113	0.156

3.2 Implementation of the pin kinetic on Abaqus/explicit

Pin kinetic is implemented in Abaqus© by means of a VUAMP subroutine (vectorized user amplitude) which specifies the amplitude of a force applied on the top of the pin (Fig. 7). This force accelerates the pin to the prescribed impact velocity (Fig. 8). After impacts, the force brakes the pin, which is then maintained at its initial position awaiting for the next impact. Such program enables to replicate the typical impact pattern identified previously (Fig. 2). To avoid with instabilities and to reduce computational effort, pin is modeled as rigid body.

As maximum contact force during impact is measured with strain gages, impact velocity can be deduced using a correlation (Eq. 5). The latter is obtained using a 2D axisymetric FEM model to simulate the impact of a linear elastic pin on a linear elastic specimen for different impact velocity (from 0.5 to 5 m/s). Despite the simple assumptions, an impact velocity V_i of 2.745 m/s [33] during primary impact was determined what is consistent with the previously estimated range of 2.0 to 3.5 m/s [22]. Due to plastic deformation, lower contact forces are expected in the numerical simulation.

$$F_{c_{max}} = 6.754 \times 10^{-5}.V_i^2 + 1.147.V_i \qquad (5)$$
$$R^2 = 0.9992$$

$F_{c_{max}}$ Maximal contact force (N) during impact
V_i Impact velocity (mm/s) of the pin

Table 3 Parameters of the Ramaswamy–Stouffer based model

E	210	(GPa)	n	0.002191526	(−)
ν	0.3	(−)	a	1.074105	(−)
D_0	$6.051915\ 10^9$	(s^{-1})	m_1	28.54772	(−)
z_0	$1.122923\ 10^{15}$	(MPa)	m_2	1	(−)
k_{10}	92	(MPa)	C_1	130,000	(MPa)
k_{11}	219.1526	(MPa)	γ_1	402.532	(−)
k_{20}	0	(MPa)	C_2	1967.677	(MPa)
k_{21}	0	(MPa)	γ_2	25	(−)

The numbers of secondary impacts and their respective impact velocity were deduced from the typical impact pattern (Fig. 4). The highest compressive force peaks correspond probably to primary impacts. Within them, it is assumed that pin is rebounding between the work piece and the actuator of the HFMI device. Four secondary impacts (red marked in Fig. 4) are thus obtained. Such approach is however questioned by the odd number of peaks in the typical pattern. Additional investigations of the pin kinematic by means of high-speed camera are needed. Analysis of the strain gage signal gives valuable information for the choice of the frame rate. Duration between two consecutive impacts is assumed constant and set to 2.22×10^{-3} s so that the frequency of primary impacts and secondary impacts of is 450 Hz.

To simulate the HFMI process, 50 primary impacts are modeled and a feed rate of 0.2 mm/hit is chosen (0.04 mm/hit when considering the primary impacts and its four secondary impacts). To avoid mesh distortion, displacement of the pin along the treatment line is driven by a VDISP subroutine (Fig. 8). It prescribes translational boundary conditions and moves the pin only when its tip is not in contact with the specimen (Table 2).

The pin has a mass of 0.03 kg. In order to see the influence of secondary impacts, three different pin kinetic schemes are investigated (Table 3). "50SP" corresponds to the typical impact period with four secondary impacts. "50HS V2745" does only simulate primary impacts with V_i=2.745 m/s and 50HS V3229 with V_i=3.229 m/s. This value was chosen so that the kinetic energy of the pin before impacts equals the one over an impact period (50SP). It is worth noticing that primary impact accounts for 72% of the total kinetic energy.

3.3 Material modeling

Linear elastic–non-linear-combined kinematic-isotropic hardening laws with strain-rate dependency are implemented. One is based on Chaboche model [31] (Eqs. 6, 7 and 8). It was calibrated by Foehrenbach [21, 22]. The isotropic portion of hardening in this model is defined by tabular data. This makes it possible to define high stress values for high plastic strains, illustrated in [21]. The

Fig. 9 **a** Comparison between experimental determined stress-strain hysteresis loop and calculated data of the model implemented by Foehrenbach [21] (CH) and by Maciolek [32] (RW). **b** Comparison of strain-rate-dependent yield for both models
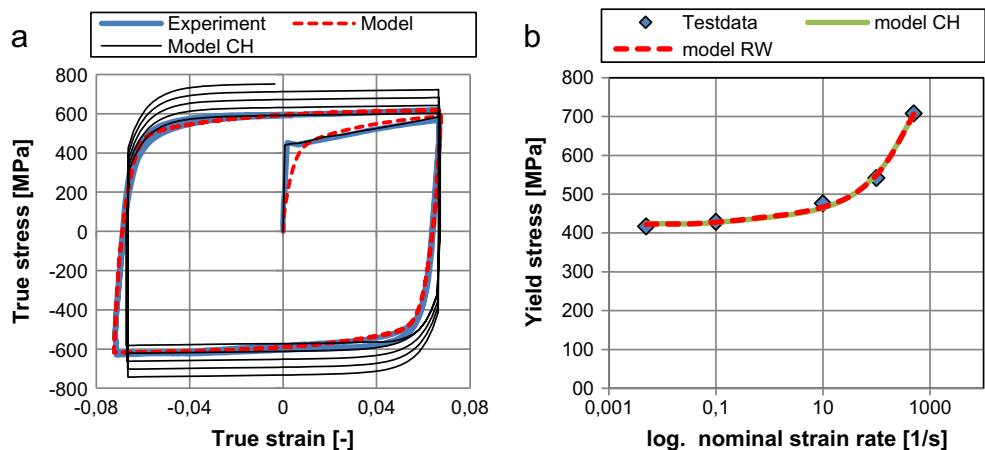
kinematic portion of hardening is defined by two terms of the back stress law (Eq. 8). The second one is based on Ramaswamy–Stouffer model [35] (Eqs. 9, 10, 11, 12, 13, and 14). It was calibrated (Table 2) and implemented by Macioleck [36] by means of a VUMAT subroutine (vectorized user material). Comparison of both models with experimental data is shown in Fig. 9a. As shown, the high portion of isotropic hardening for the Chaboche model leads to increasing stress values in hysteresis above the maximum of the experimental determined stress of around 620 MPa. Different formulation of strain-rate-dependent yield for both models leads to nearly the same results, illustrated in Fig. 9b.

Chaboche model

$$F = J_2(\sigma - \Omega) - X_i - \sigma_0 \tag{6}$$

$$\overline{\dot{\varepsilon}^p} = \frac{3}{2}\lambda \frac{\sigma' - \Omega'}{J_2(\sigma - \Omega)} \tag{7}$$

$$\dot{\Omega}_i = \frac{C_i}{\sigma_0}(\sigma - \Omega)\overline{\dot{\varepsilon}^p} - \gamma_i \Omega_i \overline{\dot{\varepsilon}^p} + \frac{\dot{C}_i}{C_i}\Omega_i \tag{8}$$

F Yield surface

σ	Stress tensor
σ'	Deviatoric part of the stress tensor
Ω	Back stress tensor
Ω'	Deviatoric part of the back stress
X_i	Isotropic hardening variable
σ_0	Yield stress
$\dot{\varepsilon}^p$	Plastic strain-rate tensor
λ	Plastic multiplier
Ω_i	ith contribution to back stress tensor
C_i	Coefficient for kinematic hardening
γ_i	Coefficient for kinematic hardening

Ramaswamy–Stouffer model

$$\dot{\varepsilon}^p_{eq} = \frac{2}{\sqrt{3}}D_0\exp\left[-\frac{a}{2}\left(\frac{Z}{\langle\Sigma_{eq}-k\rangle}\right)^{2n}\right]N \tag{9}$$

$$Z_0 = Z(t=0) \tag{10}$$

$$k_i(t) = k_{k1} - (k_{i1} - k_{i0})e^{-m\varepsilon^p_{eq,\ acc}} \tag{11}$$

$$k_{i0} = k_i(t=0) \tag{12}$$

$$k_{i1} = \lim_{t\to\infty} k_i(t) \tag{13}$$

$$\dot{\Omega}_i = C_i\dot{\varepsilon}^p - \gamma_i\Omega_i\dot{\varepsilon}^p_{eq} \tag{14}$$

Fig. 10 Residual stresses in the transverse direction determined by X-ray and neutron diffraction at specimen treated with a travel speed V_f of 12 cm/min and determined by numerical simulation when using the Ramaswamy–Stouffer model for each of the three previously described pin kinetic schemes
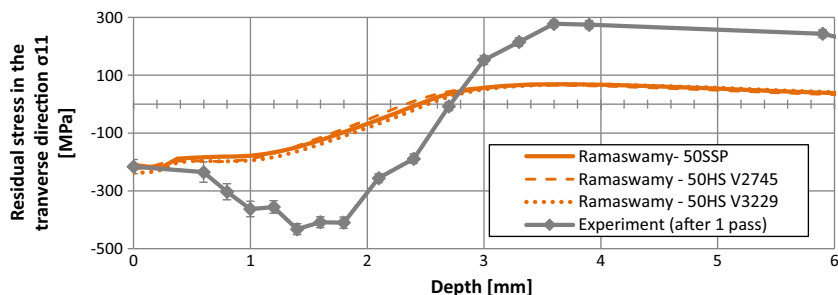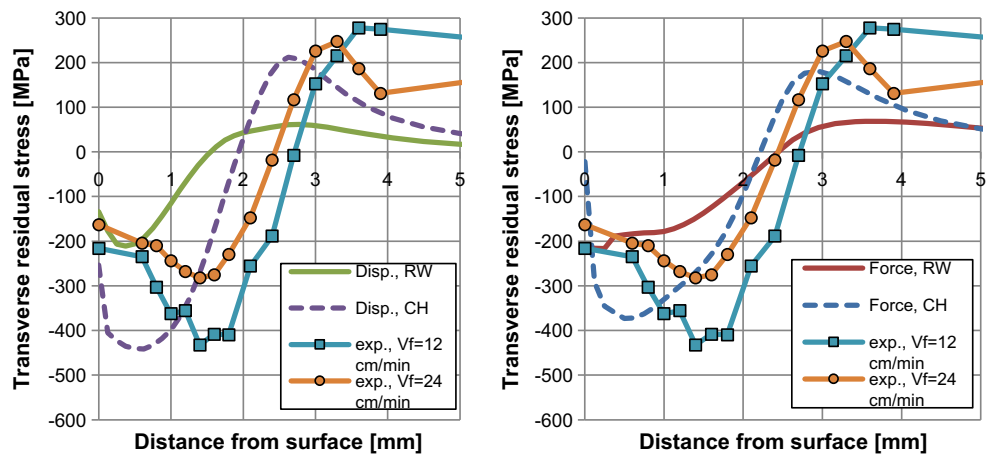
Fig. 11 Residual stress field in the transverse direction determined by X-ray and neutron diffraction (exp.) at specimens treated with a travel speed V_f of 12 cm/min and 24 cm/min and by force-controlled simulation (Force) and displacement-controlled simulation (Disp.) for the constitutive models implemented by [21] (CH) and [32] (RW)

| D_0 | Constant (sets the upper boundary strain rate when flow stress $\rightarrow \infty$) |
a	Coefficient for strain-rate sensitivity
n	Exponent for strain-rate sensitivity
Z	Drag stress
Z_0	Initial drag stress
Σ_{eq}	Uniaxial equivalent overstress tensor
N	Exterior normal to the yield surface tensor
k	Mass for isotropic hardening
k_i	ith contribution to isotropic hardening
k_{i0}	Initial static yield stress of k_i part
k_{i1}	Ultimate static yield stress k_i part
m_i	Exponent for the k_i isotropic hardening contribution

3.4 Residual stress field

Residual stress fields computed when applying the 50SP scheme are illustrated in Fig. 10. As far as the pin kinetic is concerned, marginal difference is observed between the three pin kinetic schemes (Fig. 10). It seems that secondary impacts have no significant influence on the residual field in both directions for the here-applied simulation approach.

The results of further simulations are shown in Figs. 11 and 12. In these figures, the residual stresses were averaged over multiple integration points, according to the measurement volume of the neutron diffraction measurement. The Chaboche model from [21, 22] provides qualitatively better agreements with experimental values than the Ramaswamy–Stouffer model in this investigated case. The latter has a smaller isotropic hardening term which generates smaller residual stresses. However, the agreement with the experimental determined residual stresses is higher for surface-near values (only in the transverse direction), especially compared to the FC simulation.

A major difference between the two models is the presence of tensile residual stresses in the first one to three finite elements at the surface with the Chaboche model. However, none of the investigated hardening models is able to describe the complete residual stress field in a sufficient way.

Fig. 12 Residual stress field in the longitudinal direction determined by X-ray and neutron diffraction (exp.) at specimens treated with a travel speed V_f of 12 cm/min and 24 cm/min and by force-controlled simulation (Force) and displacement-controlled simulation (Disp.) for the constitutive models implemented by [21] (CH) and [32] (RW)
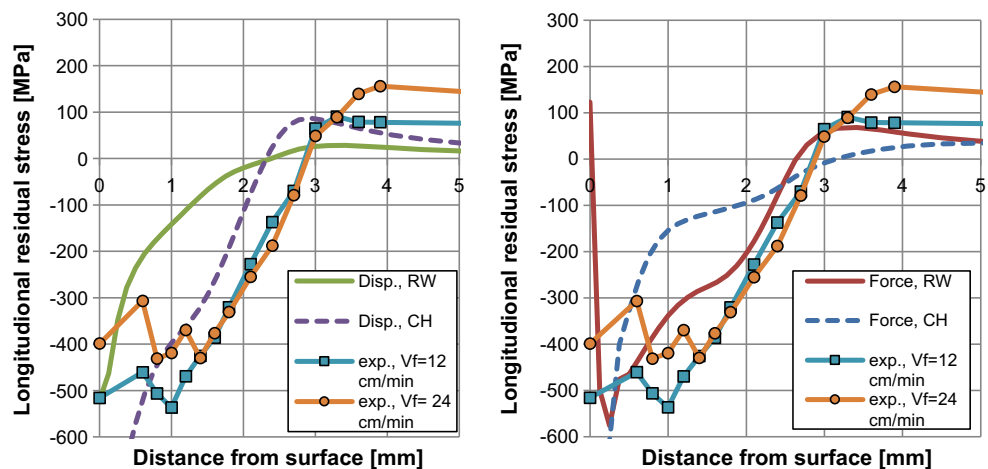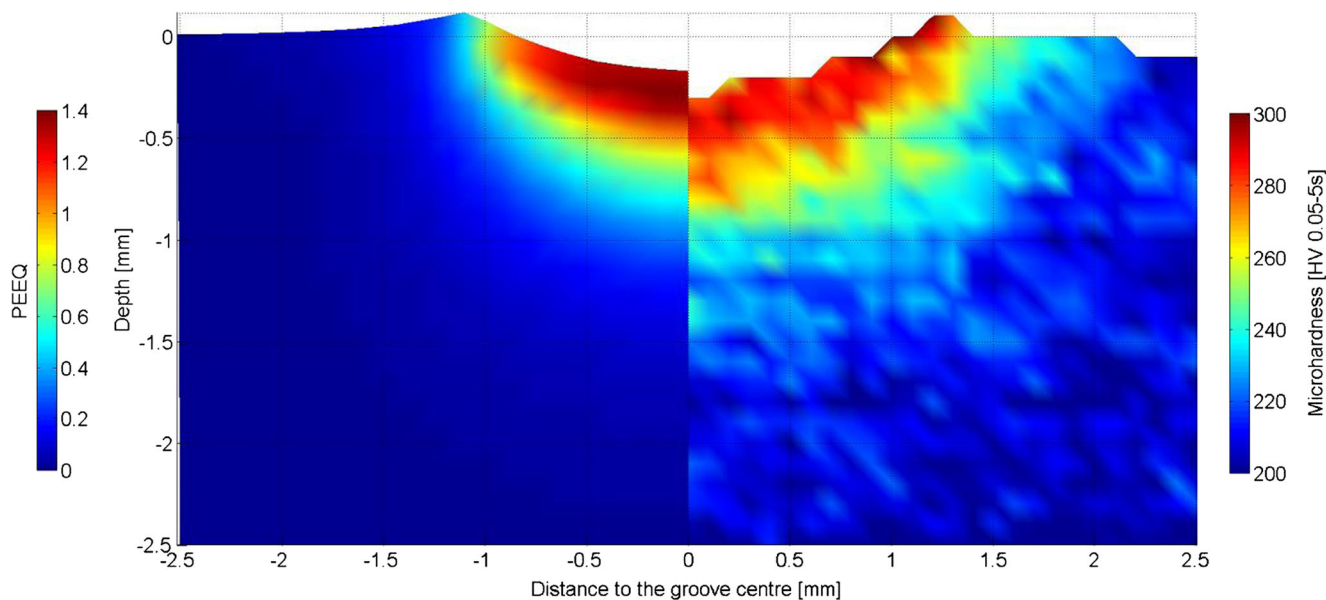
Fig. 13 Qualitative comparison of the equivalent plastic strain PEEQ computed by Abaqus© (Ramaswamy—50SP) with micro-hardness mapping (S355 J2 base material, one-time-treated)

3.5 Equivalent plastic strain

It is well-known that the residual stress sensitivity increases with an increasing materials strength [37]. From other investigations of mechanical surface treatment processes, it is known that residual stresses mostly relax during cyclic loading depending on the load level [38]. The increase of fatigue strength of these steel grades after mechanical surface treatment is mostly attributed to the work hardening close to the surface. Thus, the work-hardening effect has not been studied deeply yet. To describe the quality of the process, it is also important to define an indicator for the increase of local material's strength (Fig. 13). Usually, correlations between hardness measurements and ultimate tensile strength were used for this purpose [39]. However, the investigations of [40] show that there exists a qualitatively agreement between

equivalent plastic strain evaluated from numerical simulation and local material strength (Fig. 14).

In this work, the equivalent plastic strain computed by Abaqus© (PEEQ) is studied at the middle of the groove. This location corresponds to the one used for micro-hardness measurements. A qualitative comparison of the distribution of PEEQ with micro-hardness is performed by facing both results as illustrated on Fig. 13. However, the investigated specimen is most probably not residual stress free. Surface compressive residual shown in Figs. 11 and 12 of 200 MPa or more must be assumed. According to [41], this results in a hardness increase of 12 HV0.1 per 100 MPa compressive residual stress.

Figure 14 shows the qualitatively comparison between experimental determined hardness increase depth profile and equivalent plastic strain evaluated from numerical simulation. The hardness of the untreated material was

Fig. 14 Experimental determined hardness increase in the middle of the treated groove (Fig. 13) at specimens treated with a travel speed V_f of 12 cm/min and 24 cm/min and equivalent plastic strain by force-controlled simulation (Force) and displacement-controlled simulation (Disp.) for the constitutive models implemented by [21] (CH) and [32] (RW)
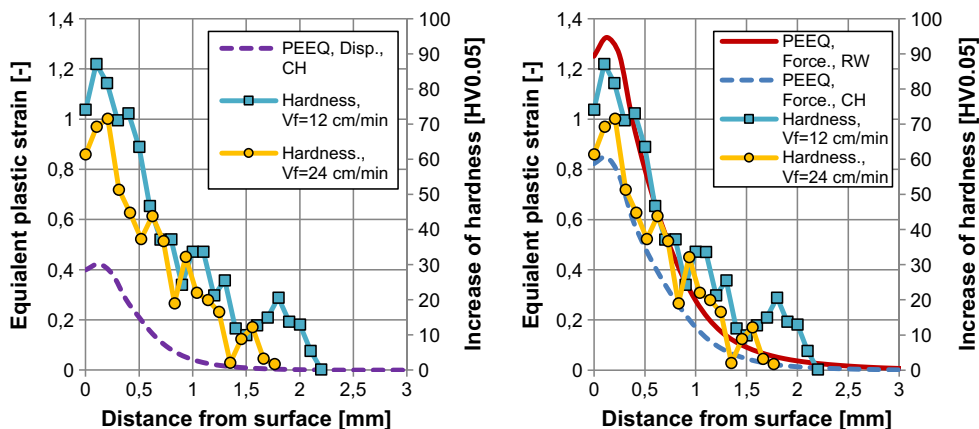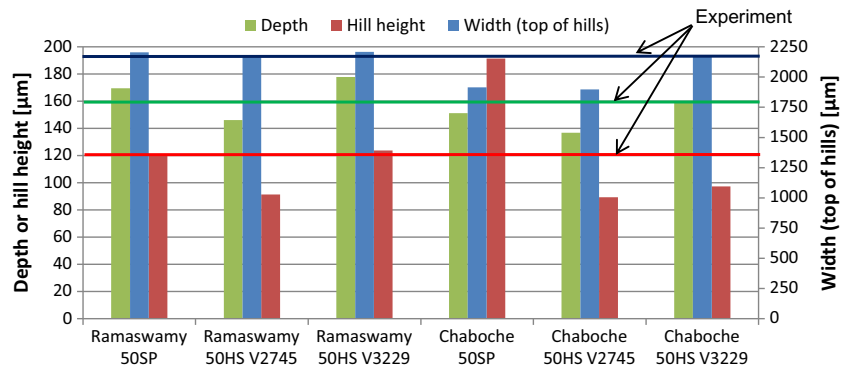
Fig. 15 Groove dimensions from the numerical simulation and the experiment

205 HV0.05 in average. The maximum increase of hardness was 87 HV0.05 for a travel speed of V_f=12 cm/min and of 69 HV for a travel speed of V_f=24 cm/min. The hardened zones reach until 2-mm depth and are in qualitative good agreement with the numerical simulation.

3.6 Groove geometry

Groove dimensions are measured on the FE model using a path of 30 nodes. Mean values are summarized in Fig. 15. Pin kinetic and material models influence the groove geometry. As shown, the groove depth varied around + 12 to − 15% depending on the hardening and load models. The hill height varies from + 60 to − 24%. Only the groove width, which is already defined by the tool shape, showed similar values for all investigated cases.

4 HFMI simulation of welded joint

The welding process causes residual stresses in the structure, which is superimposed by the acting operational loads. Hence, the effective maximum local stress in the structure increases. Additionally, the weld toe can represent a sharp notch. These phenomena cause a reduced fatigue life time of welded structures in comparison to the base metal.

A half symmetrical (y-z-plane as symmetry plane) model according to the former analysis of [19] of the welded

specimen was used for the simulations. The length of the weld seam of the specimen is 80 mm. The high-frequency hammer peening treatment was applied onto the inner $d = 60$ mm in Z-direction shown in Fig. 16, of the weld toe with FCS and an impact velocity of $V_i = 2.735$ m/s. Totally, 300 impacts were modeled ($V_i = 0.2$ mm per hit) in a dynamic explicit analysis according to [16, 21] resulting in a high calculation time of 110 h with 14 parallel cores. Pin radius was $R = 2$ mm and the pin mass was 0.03 kg. The weld toe radius was 0.3 mm and the weld opening angle 150°. The tilt angle α of the pin was 15°. The mesh around the weld toe radius was 85 μm × 400 μm × 200 μm in X/Y/Z-direction. Totally, 134,680 C3D8 elements were used for the model.

A thermo-mechanical coupled structural weld simulation utilizing the software tool Sysweld® is performed to predict the residual stress field due to welding. Based on non-destructive laser-confocal measurements of micrographs, the weld toe is modeled with a radius of $r = 0.3$ mm. According to real weld process settings, an energy input per unit length of $E = 8.0$ kJ/cm and a welding speed of $v = 60.0$ cm/min are defined. Tacking points and padding supports are included in the simulation model. The heat source of the metal active gas (MAG) welding process is modeled by a double ellipsoid according to Goldak [43]. The maximum of the heat source density is localized in the center and normally distributed. A transient temperature distribution including the time-temperature-depended phase transformation is
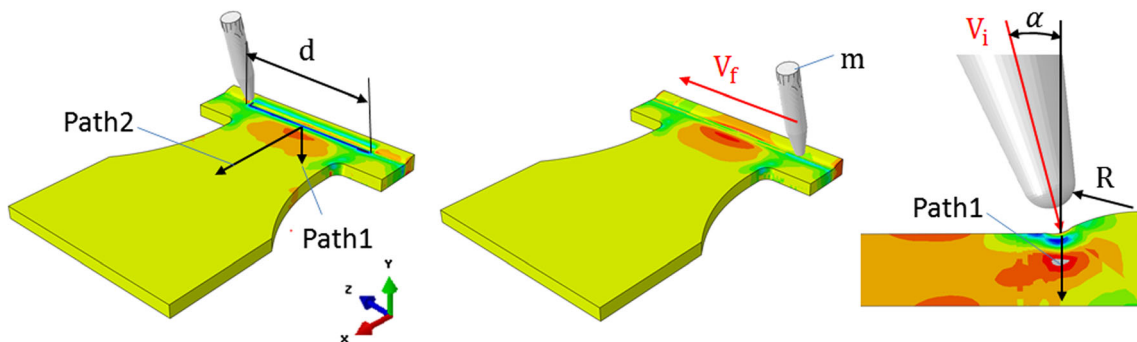

Fig. 16 HFMI simulation of single-pass butt weld

Fig. 17 Residual stress distribution over depth (**a**) and transverse to the peening direction at the surface (**b**) in the middle of the specimen in as-welded condition (AW), and after the HFMI treatment with isotropic hardening with welding residual stress (with RS) and without welding residual stress (without RS) for two evaluation paths (see Fig. 16)
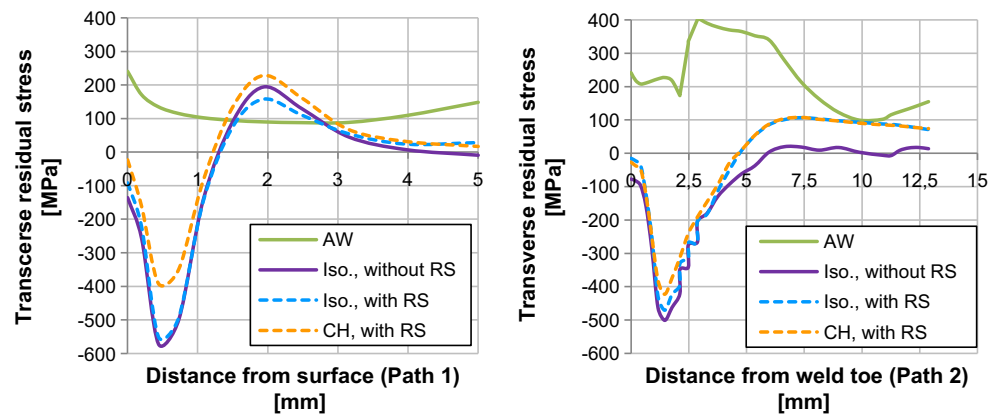
numerically calculated followed by a mechanical computation to obtain the final residual stress condition after cooling down. Additionally, regions of different microstructures and characteristics of the elastic-plastic stress-strain curves are evaluated by simulation. The material database of the applied mild construction steel S355 is implemented in Sysweld®, and isotropic hardening is used. Preliminary work by Sakketiettibutra et al. [44] compared different hardening models for structural weld simulation. Thereby, isotropic hardening showed sound accordance for mild steel in comparison to residual stress measurements. Similar simulations with kinematic hardening lead to non-conservative estimation of the residual stresses due the material- and temperature dependence of the Bauschinger effect [45]. The resulting residual stress distribution and phase-dependent material cards are subsequently transferred from Sysweld® to Abaqus®. Preliminary works, investigating the effect of different hardening laws on the final residual stress distribution after HFMI treatment, showed that the best agreement between experimental and numerical determined residual stress values is reached for a combined hardening model for mild steel applications [19].

The residual stress distribution after the HFMI treatment over the depth of the specimen (Path1) and in longitudinal to the peening direction (Path2) is illustrated in Fig. 17. The permanent indentation depth reached in this simulation was $u = 0.107$ mm averaged over 50-mm path distance in the middle of the specimen. In comparison with further simulation of flat specimen with $u = 0.25$ mm [16] and welded specimen with $u = 0.131$ [42], the treatment intensity is comparably low. No significant difference of u was determined between the used hardening models. Furthermore, the differences between the residual stress distribution with and without welding residual stresses for pure isotropic hardening reach not more than 45 MPa in depth and 60 MPa in transverse direction in the compressive residual stress zone.

5 Conclusion

The measurements of the pin kinematic during HFMI treatment with the tool Pitec Weld Line 10 performed with strain gages at manual operation [21] and with fixed tool [19] were analyzed in this work. The statistically evaluation shows that the scatter of the impact force (and thus impact energy) is significantly lower by peening with fixed tool. In direct comparison of both measurements, the impact force is significantly higher for utilizing a fixed tool, illustrated in Fig. 4. These findings reveal that an automatic process is perhaps more effective.

Furthermore, the strain gage measurements during treatment performed by [21] indicate that there occur several multiple impacts, consequently of each primary impact (frequency 90 Hz, controlled by programmable logic controller) resulting in an effective impact frequency of 450 Hz. This impact pattern was statistically analyzed correlated with an impact velocity according to Eq. 5. The impact velocity was set as input for the subsequent dynamic numerical simulation of the HFMI treatment of flat S355 J2 steel specimen, investigated by [21]. Although, the primary impacts contain around 27% of the impact energy of the complete process, no significant difference could be determined between the residual stress depth profiles from the analysis with and without the consideration of secondary impacts for the used combined non-linear isotropic kinematic hardening model with strain-rate dependency.

The numerically determined residual stress profiles were compared with the residual stress profiles determined by X-ray and neutron diffraction. A better agreement at the surface in transverse and longitudinal direction is reached for the Ramaswany–Stouffer model [35] modified by [36] and parameterized by [33]. Over the complete residual stress profile in depth, a better agreement with the Chaboche model [31] parameterized by [21] could be reached. However, none of the investigated simulation approaches describes the complete residual stress field in a sufficient way, even if the surface stress values showed the best agreement with the experimental determined values.

In the last step, this simulation procedure was transferred to a representative butt-welded joint investigated by [19]. Due to a fixed limited stable time increment of the dynamic explicit analysis, the simulation of 300 impacts over a distance of 60 mm for the designated weld takes around 110 h with 14 cpus. However, the results highlight that the highest compressive residual stresses at the surface are induced at a distance of 1.5 mm from the weld toe radius. The presence of welding residual stresses had a mostly negligible effect of the residual stress after treatment.

As a conclusion, a way of characterizing the pin kinetic during HFMI treatment from strain gage signal was presented. One the one hand, such a method provides indication of the treatment quality. The set frequency (i.e., primary impacts frequency) can be controlled, and the repeatability of the pin kinetic is assessed. On the other hand, it enables a better description of the treatment condition. For the probed HFMI device and treatment conditions, the presence of secondary impacts was indeed highlighted and the pin impact velocity was estimated consistently with previous high-speed camera measurements [22]. However, uncertainties remain, in particular concerning the exact number of secondary impacts. High-speed camera captures should be removed, provided that a sufficient sampling frequency is set. To this purpose, the present method seems to be an appropriate preliminary study. The found pin kinetic was implemented in numerical simulations to evaluate its effects on two major aspects for the prediction of the fatigue strength of welded joints: groove geometry and residual stress state. For the investigated conditions, secondary impacts show at first sight a greater influence on groove geometry than on residual stresses, which stay almost unchanged. The performed process simulation in this work is a first step for the prediction of the residual stress state after HFMI treatment. It is clearly shown that the numerical calculation of the HFMI-induced residual stresses is still a challenging task, even with an extensive investigation of the load history and with the implementation advanced materials models.

References

1. Statnikov E, Trufyakov VI, Mikheev PP, Kudryavtsev YF (1996) Specification for weld toe improvement by ultrasonic impact treatment, IIW, Paris, Doc. XIII-1617-96

2. Yildirim HC, Marquis GB, Barsoum Z (2013) Fatigue assessment of high frequency mechanical impact (HFMI)-improved fillet welds by local approaches. Int J Fatigue 52:57–67. https://doi.org/10.1016/j.ijfatigue.2013.02.014

3. Yildirim HC, Marquis GB (2012) Fatigue strength improvement factors for high strength steel welded joints treated by high frequency mechanical impact. Int J Fatigue 44:168–176. https://doi.org/10.1016/j.ijfatigue.2012.05.002

4. Marquis GB, Mikkola E, Yildirim HC, Barsoum Z (2013) Fatigue strength improvement of steel structures by high-frequency mechanical impact: proposed fatigue assessment guidelines. Weld World 57:803–822. https://doi.org/10.1007/s40194-013-0075-x

5. Marquis G, Barsoum Z (2014) Fatigue strength improvement of steel structures by high-frequency mechanical impact: proposed procedures and quality assurance guidelines. Weld World 58:19–28. https://doi.org/10.1007/s40194-013-0077-8

6. Yildirim HC (2013) Design aspects of high strength steel welded structures improved by high frequency mechanical impact (HFMI) treatment. Doctoral Thesis, Aalto University. Department of Applied Mechanics

7. Yıldırım HC, Marquis GB (2014) Fatigue design of axially-loaded high frequency mechanical impact treated welds by the effective notch stress method. Mater Des 58:543–550. https://doi.org/10.1016/j.matdes.2014.02.001

8. Haagensen PJ, Maddox SJ (2011) IIW recommendations on post weld fatigue life improvement of steel and aluminium structures. International Institute of Welding, Paris

9. Nüsse G (2011) REFRESH—Lebensdauerverlängerung bestehender und neuer geschweißter Stahlkonstruktionen / REFRESH—Extension of the fatigue life of existing and new welded steel structures. Verlag und Vertriebsgesellschaft GmbH, Düsseldorf

10. Le Quilliec G, Lieurade H-P, Bousseau M, Drissi-Habti M, Inglebert G (2011) Fatigue Behaviour of Welded Joints Treated by High Frequency Hammer Peening: Part I, Experimental Study. 64th Annual Assembly International Conference of the International Institute of Welding (IIW 2011), Jul 2011, Chennai, India

11. Tehrani Yekta R, Ghahremani K, Walbridge S (2013) Effect of quality control parameter variations on the fatigue performance of ultrasonic impact treated welds. Int J Fatigue 55:245–256. https://doi.org/10.1016/j.ijfatigue.2013.06.023

12. Berg J, Stranghoener N (2014) Fatigue strength of welded ultra high strength steels improved by high frequency hammer peening. Procedia Mater Sci 3:71–76. https://doi.org/10.1016/j.mspro.2014.06.015

13. Leitner M, Gerstbrein S, Ottersböck MJ, Stoschka M (2015) Fatigue strength of HFMI-treated high-strength steel joints under constant and variable amplitude block loading. Procedia Eng 101:251–258. https://doi.org/10.1016/j.proeng.2015.02.036

14. Lefebvre F, Revilla-Gomez C, Buffière JY, Verdu C, Peyrac C (2014) Understanding the mechanisms responsible for the beneficial effect of hammer peening in welded structure under fatigue loading. Adv Mater Res 996:761–768

15. Weich I (2008) Ermüdungsverhalten mechanisch nachbehandelter Schweißverbindungen in Abhängigkeit des Randschichtzustands / Fatigue behaviour of mechanical post weld treated welds depending on the edge layer condition / Technical University of Braunschweig. Doctoral Thesis

16. Hardenacke V, Farajian M, Siegele D (2014) Modelling and simulation of the high frequency mechanical impact (HFMI) treatment of welded joints. In: Proc. of 67th IIW Annual Assembly & International Conference 2014. International Institute of Welding, Paris, Frankreich XIII-2533-14 1-10

17. Le Quilliec G, Lieurade H-P, Bousseau M, Drissi-Habti M, Inglebert G (2011) Fatigue Behaviour of Welded Joints Treated by High Frequency Hammer Peening: Part II, Numerical study. 64th Annual Assembly International Conference of the International Institute of Welding (IIW 2011), Jul 2011, Chennai, India

18. Baptista R, Infante V, Branco C (2011) Fully dynamic numerical simulation of the hammer peening fatigue life improvement technique. Procedia Eng 10:1943–1948. https://doi.org/10.1016/j.proeng.2011.04.322

19. Simunek D, Leitner M, Stoschka M (2013) Numerical simulation loop to investigate the local fatigue behaviour of welded and HFMI-treated joints. IIW Doc WIII-WG2–136-13

20. Guo C, Hu S, Wang D, Wang Z (2015) Finite element analysis of the effect of the controlled parameters on plate forming induced by ultrasonic impact forming (UIF) process. Appl Surf Sci 353:382–390. https://doi.org/10.1016/j.apsusc.2015.06.094

21. Foehrenbach J, Hardenacke V, Farajian M (2016) High frequency mechanical impact treatment (HFMI) for the fatigue improvement: numerical and experimental investigations to describe the condition in the surface layer. Weld World 60:749–755. https://doi.org/10.1007/s40194-016-0338-4

22. Foehrenbach J (2015) Fatigue life prediction of high frequency mechanical impact treated welded joints by numerical simulation and damage mechanic approaches. Master Thesis, Offenburg University of Applied Science

23. Quilliec GL, Lieurade H-P, Bousseau M et al (2013) Mechanics and modelling of high-frequency mechanical impact and its effect on fatigue. Weld World 57:97–111. https://doi.org/10.1007/s40194-012-0013-3

24. Hu S, Guo C, Wang D, Wang Z-J (2016) 3D dynamic finite element analysis of the nonuniform residual stress in ultrasonic impact treatment process. J Mater Eng Perform 25:4004–4015. https://doi.org/10.1007/s11665-016-2206-1

25. Khurshid M, Leitner M, Barsoum Z, Schneider C (2017) Residual stress state induced by high frequency mechanical impact treatment in different steel grades—numerical and experimental study. Int J Mech Sci 123:34–42. https://doi.org/10.1016/j.ijmecsci.2017.01.027

26. Yuan K, Sumi Y (2016) Simulation of residual stress and fatigue strength of welded joints under the effects of ultrasonic impact treatment (UIT). Int J Fatigue 92:321–332. https://doi.org/10.1016/j.ijfatigue.2016.07.018

27. Deng C, Liu Y, Gong B, Wang D (2016) Numerical implementation for fatigue assessment of butt joint improved by high frequency mechanical impact treatment: a structural hot spot stress approach. Int J Fatigue 92:211–219. https://doi.org/10.1016/j.ijfatigue.2016.07.008

28. Yang X, Zhou J, Ling X (2012) Study on plastic damage of AISI 304 stainless steel induced by ultrasonic impact treatment. Mater Des 1980-2015 36:477–481. https://doi.org/10.1016/j.matdes.2011.11.023

29. Guo C, Wang Z, Wang D, Hu S (2015) Numerical analysis of the residual stress in ultrasonic impact treatment process with single-impact and two-impact models. Appl Surf Sci 347:596–601. https://doi.org/10.1016/j.apsusc.2015.04.128

30. Marquis GB, Barsoum Z (2016) IIW recommendations for the HFMI treatment: for improving the fatigue strength of welded joints. Springer, Singapore

31. Chaboche JL (1986) Time-independent constitutive theories for cyclic plasticity. Int J Plast 2:149–188. https://doi.org/10.1016/0749-6419(86)90010-0

32. Johnson GR, Cook WH (1983) A Constitutive Model and Data for Metals Subjected to Large Strains, High Strain Rates, and High Temperatures. Proceedings 7th International Symposium on Ballistics, The Hague, 19–21 April 1983, p 541–547

33. Ernould C (2017) Numerical simulation of pin kinetic and its influence on the material hardening, residual stress field and topography during high frequency mechanical impact (HFMI) treatment. Master Thesis, Karlsruhe Institute of Technology

34. Simunek D (2013) Implementierung der Schweißnahtnachbehandlung mittels eines hochfrequenten Hämmerverfahrens in die numerische Lebensdauerabschätzung. Master Thesis, Montanuniversität Leoben—Chair of Mechanical Engineering

35. Ramaswamy GV (1985) A constitutive model for the inelastic multiaxial cyclic response of a nickel base superalloy Rene 80. Doctoral Thesis, University of Cincinnati—Department of aerospace engineering and engineering mechanics

36. Maciolek A (2017) Implementierung eines elasto-viskoplastichen Materialmodells zur Simulation des Kugelstrahlens an Komponenten aus 42CrMoS4. Master Thesis, Karlsruhe Institute of Technology

37. Macherauch E, Wohlfahrt H (1985) Eigenspannungen und Ermüdung. In: Munz D (ed) Ermüdungsverhalten metallischer Werkstoffe. DGM Informationsgesellschaft GmbH, Oberursel, pp 237–283

38. Schulze V (2006) Modern mechanical surface treatment: states, stability, effects. Wiley-VCH, New York

39. International Organization for Standardization (2013) ISO 18265: 2013-10 (EN), Metallic materials—conversion of hardness values

40. Muller M, Barrans SM, Blunt L (2011) Predicting plastic deformation and work hardening during V-band formation. J Mater Process Technol 211:627–636. https://doi.org/10.1016/j.jmatprotec.2010.11.020

41. Scholtes B, Vöhringer O (1989) Grundlagen der mechanischen Oberflächenbehandlung. In: Schütz W (ed) Mechanische Oberflächenbehandlung: Festwalzen-Kugelstrahlen-Sonderverfahren. DGM Informationsgesellschaft GmbH, Oberursel, pp 3–20

42. Schubnell J, Hardenacke V, Farajian M (2017) Strain-based critical plane approach to predict the fatigue life of high frequency mechanical impact (HFMI)-treated welded joints depending on the material condition. Weld World 61:1199–1210. https://doi.org/10.1007/s40194-017-0505-2

43. Goldak J, Chakravarti A, Bibby M (1984) A new finite element model for welding heat sources. Metall Trans B 15:299–305. https://doi.org/10.1007/BF02667333

44. Sakketiettibutra J, Loose T, Wohlfahrt H (2009) Zur Wahl des Verfestigungsmodells bei der Berechnung von Schweißeigenspannungen. Tagungsband, Weimar, pp 21–33

45. Bauschinger J (1886) Über die Veränderung der Elastizitätsgrenze und die Festigkeit des Eisens und Stahls durch Strecken und Quetschen, durch Erwärmen und Abkühlen und durch oftmals wiederholte Beanspruchungen. Mitteilungen des meachnisch-technischen Laboratoriums der Königlich Technichen Hochschule München, Munich